Impact of random alloy fluctuations on the carrier distribution in multicolor (In,Ga)N/GaN quantum well systems

Michael O'Donovan,[1,2,3,*] Patricio Farrell,[3] Julien Moatti,[4,5] Timo Streckenbach,[3] Thomas Koprucki,[3] and Stefan Schulz[1,2]

[1] *Tyndall National Institute, University College Cork, Cork T12 R5CP, Ireland*
[2] *School of Physics, University College Cork, Cork T12 YN60, Ireland*
[3] *Weierstrass Institute (WIAS), Mohrenstrasse 39, Berlin 10117, Germany*
[4] *Inria, Universiteé Lille, CNRS, UMR 8524—Laboratoire Paul Painlevé, Lille F-59000, France*
[5] *Institute of Analysis and Scientific Computing, Vienna University of Technology, Wiedner Hauptstr. 8-10, A-1040 Wien, Austria*

(Received 23 September 2022; revised 10 November 2023; accepted 23 January 2024; published 27 February 2024)

The efficiency of (In,Ga)N-based light-emitting diodes (LEDs) is limited by the failure of holes to evenly distribute across the (In,Ga)N/GaN multiquantum well stack that forms the active region. To tackle this problem, it is important to understand carrier transport in these alloys. In this work, we study the impact that random alloy fluctuations have on the distribution of electrons and holes in such devices. To do so, an atomistic tight-binding model is employed to account for alloy fluctuations on a microscopic level and the resulting tight-binding energy landscape forms input to a quantum corrected drift-diffusion model. Here, quantum corrections are introduced via localization-landscape theory. Similar to experimental studies in the literature, we have focused on a multiquantum well system in which two of the three wells have the same In content, while the third well differs in In content. By changing the order of wells in this "multicolor" quantum well structure and looking at the relative radiative-recombination rates of the different emitted wavelengths, we (i) gain insight into the distribution of carriers in such a system and (ii) can compare our findings to trends observed in experiment. We focus on three factors and evaluate the impact that each have on carrier distribution: an electron blocking layer, quantum corrections, and random alloy fluctuations. We find that the electron blocking layer is of secondary importance. However, in order to recover experimentally observed features—namely, that the p-side quantum well dominates the light emission—both quantum corrections *and* random alloy fluctuations should be considered. The widely assumed homogeneous virtual-crystal approximation fails to capture the characteristic light emission distribution across a multiquantum well stack.

DOI: 10.1103/PhysRevApplied.21.024052

I. INTRODUCTION

At the heart of modern light-emitting diodes (LEDs) operating in the blue-to-violet spectral region are (In,Ga)N/GaN multiquantum well (MQW) systems [1]. While the efficiency of these LEDs is and can be high, pushing the emission to longer visible wavelengths (with higher InN content) or to ultraviolet wavelengths (with (Al,Ga)N alloys) provides technological challenges [2,3]. In general, understanding the carrier distribution can help to guide maximizing the efficiency in an LED, since ideally the carriers will be distributed evenly across the entire MQW region, so that all QWs will contribute to emission [4]. However, previous experimental studies on carrier distribution in (In,Ga)N/GaN MQW systems have indicated that mainly the well closest to the p-doped contact side contributes to the light emission process [4–7]. To do so samples were specifically designed to gain insight into the carrier distribution inside the active region of an LED. Overall, this has been attributed to a sequential filling of the QWs, resulting in a high hole density only in the p-side QW. To establish accurate carrier-transport models, the trends found in the experimental studies of Refs. [4–7] should ideally be predicted, without introducing extra free parameters to simulation models.

Widely used one-dimensional (1D) simulation methods employing a Schrödinger-Poisson drift-diffusion approach—the workhorse of many commercial software packages—fail to predict the poor hole distribution across an (In,Ga)N MQW region [8]. Previous theoretical studies have reproduced the experimentally observed behavior; however, this has required (i) treating bound carriers in a quantum mechanical picture, (ii) softening of the QW barrier interface to account for tunneling effects,

*odonovan@wias-berlin.de

(iii) distinguishing between continuum and bound carriers in the carrier-transport model (the multipopulation model), and (iv) allowing for scattering between the different populations [8]. However, the impact of alloy disorder is basically neglected in this advanced but also complex carrier-transport model.

Alloy disorder impacts different materials in different manners. For example, dilute nitride alloys such as Ga(As,N) result in a modification of the conduction band, as the nitrogen introduces states above the conduction-band edge of GaAs. This leads to hybridization with the conduction-band edge and leads to an unusual band evolution with nitrogen content [9]. Similarly, disorder in (Ga,In)P primarily impacts the conduction-band edge [10–12]. On the other hand, atomic scale alloy disorder in III-nitride (III-N) materials such as (In,Ga)N results in a modification of states in the *valence band* [13,14]. This gives rise to carrier localization, particularly for holes, in (In,Ga)N alloys.

Experimental and theoretical studies on the electronic [15–17] and optical [18,19] properties of (In,Ga)N systems have already revealed that these properties are significantly impacted by alloy-fluctuation induced carrier-localization effects. However, the impact of alloy disorder on the carrier transport has only been targeted recently [20–25]. Here, studies are ranging from fully atomistic quantum mechanical approaches [20] up to modified continuum-based models [21–25]. Previously in the literature, transport through a disordered alloy has been addressed with a continuum approach by creating a random distribution of atoms and averaging over a volume to get a "local" alloy content [23,25]. This was then used to determine fluctuating conduction- and valence-band confining energies. In this case, there is uncertainty in the band-edge energies, which will depend on (i) the volume over which the alloy is averaged and (ii) the parameters used to calculate local strain and polarization.

To avoid these uncertainties while still accounting for alloy fluctuations in transport calculations, we have recently developed a three-dimensional (3D) multiscale simulation framework that connects atomistic tight-binding theory with a modified quantum corrected drift-diffusion (DD) solver. The tight-binding model has been extensively benchmarked against both *ab initio* theory and experiments. A comparison between the continuum based and atomistic based approaches would provide useful insight into the effectiveness of the continuum model. However, the uncertainties mentioned above make such a comparison extremely challenging. Therefore, we limit ourselves here to starting from an atomistic setting that has been suitably benchmarked.

The framework has been employed to investigate unipolar carrier transport and it has been found that alloy fluctuations result in an increase in carrier transport of electrons (in an *n*-*i*-*n* system) [21] but decrease transport in the case of holes (in a *p*-*i*-*p* systems) [22]. As the impact of alloy disorder is different for electron and hole species, one can infer that this may also impact carrier distribution in bipolar devices. In the present work, we apply our scheme to investigate the active region of (In,Ga)N-based MQW LED structures (thus *p*-*i*-*n* systems) and target a system that allows us to directly study the problem of carrier distribution across MQW systems.

In this paper, we show that when employing our quantum corrected 3D simulation framework that accounts for random alloy fluctuations, the experimentally observed trends are captured (namely, that light emission occurs mainly from the *p*-side QW) without introducing, e.g., a multipopulation scheme. This highlights that our developed procedure presents an ideal starting point for future device-design studies.

To highlight clearly the impact that 3D random alloy fluctuations have on the carrier distribution in the active region of an (In,Ga)N-based LED, we use as a reference point the virtual-crystal approximation (VCA), which can effectively be described by a 1D model. This allows us to identify 3D alloy fluctuations as a key mechanism for explaining experimental results.

Our studies show that, when using the same input parameter set, only the model accounting for random alloy fluctuations produces trends that are consistent with the experimental data. The widely employed VCA yields results that are in contradiction with the experimental data, namely, that radiative recombination stems mainly from the well *furthest away* from the *p* side. Overall, this highlights (i) that alloy fluctuations are essential to achieve an accurate description of the carrier transport and (ii) they have to be taken into account when theoretically guiding the design of energy-efficient III-N light emitters.

The paper is organized as follows. In Sec. II, we outline the model structure used for calculations and briefly summarize some of the literature experimental data from Ref. [5]. The theoretical framework that we use is outlined in Sec. III. Our results are discussed in Sec. IV. Finally, Sec. V presents our conclusions.

II. MODEL MQW STRUCTURES AND LITERATURE EXPERIMENTAL FINDINGS

To investigate the carrier distribution in (In,Ga)N/GaN MQW systems, we proceed similarly to experimental studies in the literature [5,7] and target MQW systems in which one of the wells in the MQW stack has a slightly higher In content compared to the remaining wells. In our case, we study MQW systems with three (In,Ga)N/GaN wells. Here, two are $In_{0.1}Ga_{0.9}N$ ("shallow") wells and one is an $In_{0.125}Ga_{0.875}N$ ("deep") QW. These QWs are 3 nm wide and separated by 5-nm GaN barriers. The band-edge profile of such a system along the transport (*c*) direction, using

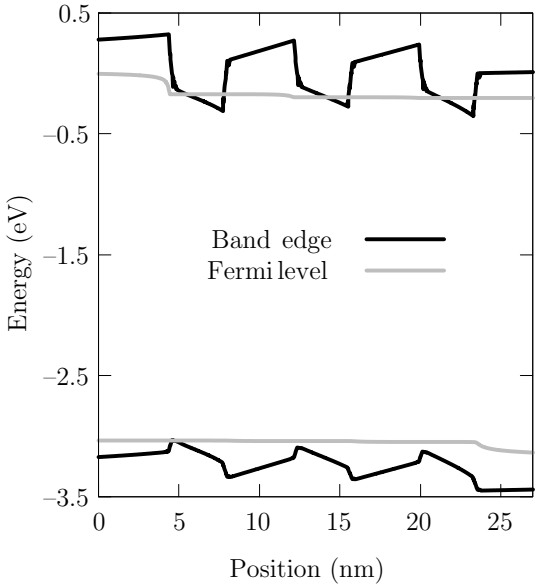

FIG. 1. Conduction- and valence-band edges (black) along with the quasi-Fermi energies for electrons and holes (gray) in an (In,Ga)N/GaN MQW system described in the virtual-crystal approximation (VCA). The band-edge profile and the quasi-Fermi levels are shown at a current density of 50 A/cm^2. The leftmost (In,Ga)N QW contains 12.5% indium, while the other two (In,Ga)N wells (center and right) contain 10% indium. The n- (p-)doped region is to the left (right) of the QWs (see Fig. 2).

a VCA, is shown in Fig. 1 at a current density of 50 A/cm^2 across the c plane.

In the following, we investigate the carrier-transport properties in two settings: (i) on an atomistic level, accounting for random alloy fluctuations, and (ii) in the frame of a VCA, thus neglecting alloy fluctuations. In the latter VCA case (ii), at a given z position (along the c direction), there is no variation in material properties within the growth plane (c plane). This assumption is also made in the widely used 1D transport simulations on (In,Ga)N MQWs.

To study the carrier distribution in MQW systems using the simulation settings (i) and (ii), we again follow the experimental approach presented in, e.g., Ref. [5] and the deep QW is moved from the n side [position 1 (n side) in Fig. 2] to the p side [position 3 (p side) in Fig. 2]. In the case of the random alloy structures, the same microscopic configuration is kept for each well and only the ordering is changed.

For each of these systems, the ratio of radiative recombination from the shallow wells to the deep well is calculated using

$$\varrho = \frac{\mathcal{R}^{RAD}_{\Omega_S}}{\mathcal{R}^{RAD}_{\Omega_D}}, \tag{1}$$

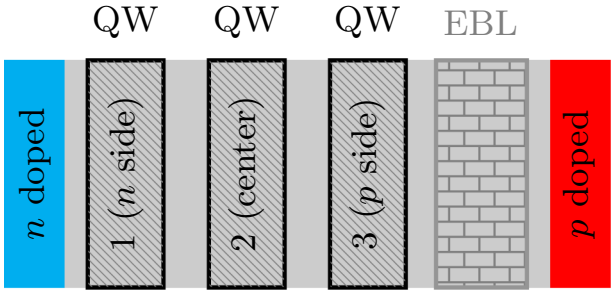

FIG. 2. A schematic illustration of the MQW system. The n-doped region is shown in blue, the p-doped region is in red, and undoped regions are in gray. The QWs are numbered starting from the n side. The electron blocking layer (EBL) is positioned at the p side, between the QWs and the n-doped region—this is absent in some of the simulations.

where

$$\mathcal{R}^{RAD}_{\Omega_i} = \int_{\Omega_i} R^{RAD}(\mathbf{r}) dV \tag{2}$$

is the total radiative recombination from the region Ω_i. Here, Ω_D is the volume containing the deep QW and Ω_S is the volume containing the shallow wells (as there are two shallow QWs, this is the union of the two shallow QW regions). Since we are studying a system with three QWs, an even distribution of carriers across the MQWs would result in a ratio of $\varrho = 2$. A small (large) value of ϱ means that emission is dominated by the deep (shallow) wells. Previous experimental work on a similar system by Galler *et. al.* [5] has found that ϱ *is small* (i.e., emission is dominated by the deep QW) *only when the deep well is closest to the p-doped side of the MQW system* [thus position 3 (p side) in Fig. 2]. The authors conclude that holes are responsible for this behavior and argue that they are mainly found in the p-side QW and not in wells further away from the p side. As a consequence, the overall emission from the (In,Ga)N/GaN MQW system is dominated by the emission from this well closest to the p-doped region. In line with Ref. [5], we calculate ϱ at a current density of 50 A/cm^2, which allows us to compare the here predicted trends with the trends found in the experimental studies. The theoretical framework employed to gain insight into ϱ is discussed in the following section.

III. THEORETICAL FRAMEWORK

In this section, we introduce the underlying (microscopic) theory of our multiscale simulations. We start in Sec. III A with the electronic structure model, an atomistic tight-binding (TB) model, and discuss the drift-diffusion approach in Sec. III B. Since all these ingredients have been discussed in detail in Refs. [21,22], here we give only a brief summary.

A. Tight-binding energy landscape

We model the electronic structure of the above-described (In,Ga)N MQW systems on an atomistic level with a nearest-neighbor sp^3 TB model [26]. Here, local strain and polarization effects are included using a valence-force-field model and local-polarization theory, respectively [27].

To connect the TB model to a DD solver, we proceed as follows. First, the TB model is used to extract a potential energy landscape describing the MQW region of the device using an atomistic framework. To do so, at each atomic site in the three-dimensional (3D) supercell, a local TB Hamiltonian is constructed from the full TB Hamiltonian [16]; a similar approach has been used to extract local band-edge profiles by Schliwa *et al.* using a $\mathbf{k}\cdot\mathbf{p}$ model and while studying strain effects in quantum dots [28]. Subsequently, only the local TB Hamiltonian is diagonalized, yielding the local confining conduction- and valence-band-edge energy at each lattice site. These local confining band-edge energies now already include effects arising from alloy fluctuations and connected fluctuations in strain and the built-in polarization field. The obtained 3D confining energy landscape, after employing a Gaussian softening, forms the basis for our DD calculations.

In previous studies, we have investigated and discussed in detail the influence of the Gaussian softening on transport calculations for electrons and holes [21,22]. Here, we choose a Gaussian broadening on the order of the GaN lattice constant, $\sigma_{c,v} = a^{\mathrm{GaN}} = 0.3189$ nm, in all calculations. This value is large enough to average over a number of neighboring sites, while also small enough to retain fluctuations in the energy landscape.

B. Device simulation

A conduction and valence band at a single atomic site itself is not physically meaningful, as the electron and hole wave functions will extend over a volume. Instead, we have calculated the local confinement potential energy, which can be used to study single-particle states via, e.g., solving the Schrödinger equation in the effective-mass approximation. This accounts for quantum corrections and is often coupled with the DD equations (which will be discussed below) to include quantum effects in a transport calculation.

Such a Schrödinger-Poisson solver is widely available in commercial software packages. However, in these packages it is largely restricted to 1D simulations, since the extension to a 3D system is computationally basically unfeasible. Instead of solving the large eigenvalue problem connected to evaluating the Schrödinger equation, we have implemented quantum corrections via localization-landscape theory (LLT) [29]. Below, using 1D quantum corrected DD calculations, we will show that this numerically more efficient LLT approach gives results similar to a fully self-consistent Schrödinger-Poisson solver.

From LLT, we extract an effective confining potential for the conduction- and valence-band-edge, starting from the TB energy landscape.

An example of the resulting quantum corrected energy landscape is given in Figs. 3(a) and 3(b). Here, in-plane band-edge profiles for a single atomic plane through an $In_{0.1}Ga_{0.9}N$ QW, after LLT has been applied, are shown. As Fig. 3(a) reveals, the fluctuations in the valence-band-edge energy due to alloy fluctuations are of the order of 100 meV. In combination with the high effective hole mass, these fluctuations are large enough to give rise to strong carrier-localization effects, as already seen in other studies [26,30,31]. We therefore expect that, especially for holes, the inclusion of random alloy fluctuations in the simulation will impact the carrier distribution. Consequently, the recombination rates are also expected to be noticeably influenced.

The variation in the conduction-band-edge energy is significantly smaller (on the order of 30 meV), as can be seen in Fig. 3(b). Since the effective electron mass is much lower in comparison with the holes, electron wave functions are less strongly perturbed by alloy fluctuations. As discussed above, this is in line with previous observations of localization in III-N alloys.

The impact that these fluctuations in the band-edge energies have on the radiative recombination is also seen in Fig. 3(c); the radiative recombination is calculated with DDFERMI, as will be described in Sec. III B. The correlation between the valence-band-edge maxima and regions of high radiative recombination can be clearly identified; similar spatial profiles can be seen for nonradiative (Auger) recombination (not shown).

In order to highlight the impact of random alloy fluctuations on carrier transport and the distribution of carriers across a MQW system, we compare our atomistic calculations with the outcome of a VCA. In the latter case, a homogeneous effective crystal is constructed, where the material properties are chosen to be interpolated properties of the binaries InN and GaN within the QW region. Here, a composition-weighted interpolation scheme is employed. A band-gap bowing of -2.0 eV is used, consistent with the underlying atomistic TB model [27]. The VCA description, without any Gaussian broadening, is similar to commercially available packages. However, and in contrast to commercial software packages, quantum corrections via LLT can also be taken into account in our VCA simulations, following the approach used for the random alloy case. The fact that a VCA can be combined with LLT to account for quantum corrections allows for a direct comparison with standard Schroedinger-Poisson solvers.

The devices are simulated in the frame of a (quantum corrected) DD model. This is evaluated on a 3D mesh,

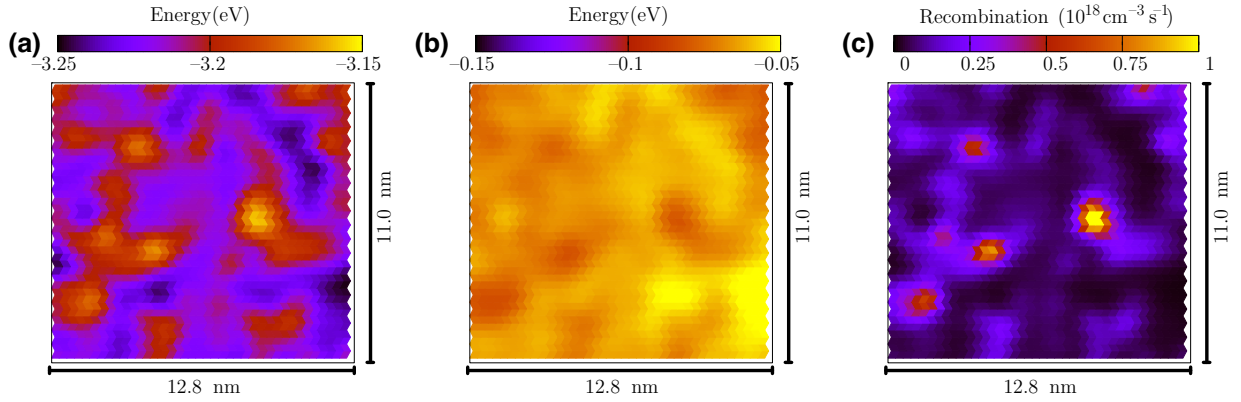

FIG. 3. The profile of (a) the valence-band-edge energy, (b) the conduction-band-edge energy, and (c) the radiative-recombination rate in the growth plane (c plane) of an $In_{0.1}Ga_{0.9}N$ QW; the current density is 50 A/cm^2 in all depicted figures. The atomic plane pictured is within the center well. The data are shown in all cases on a linear scale.

which is built from the underlying TB mesh. The mesh construction is discussed in Appendix A. The DD builds on the van Roosbroeck system of equations [32]:

$$-\nabla\cdot(\varepsilon_s(\mathbf{r})\nabla\psi(\mathbf{r})) = q(p(\mathbf{r}) - n(\mathbf{r}) + C(\mathbf{r})), \tag{3a}$$

$$\nabla\cdot\mathbf{j}_n(\mathbf{r}) = qR(\mathbf{r}), \tag{3b}$$

$$\nabla\cdot\mathbf{j}_p(\mathbf{r}) = -qR(\mathbf{r}), \tag{3c}$$

$$\mathbf{j}_n(\mathbf{r}) = -q\mu_n n(\mathbf{r})\nabla\varphi_n(\mathbf{r}), \tag{3d}$$

$$\mathbf{j}_p(\mathbf{r}) = -q\mu_p p(\mathbf{r})\nabla\varphi_p(\mathbf{r}). \tag{3e}$$

In the above equations, q is the elementary charge, $\varepsilon_s(\mathbf{r}) = \varepsilon_0\varepsilon_r(\mathbf{r})$ is the dielectric permittivity, $\psi(\mathbf{r})$ is the device electrostatic potential, $p(\mathbf{r})$ and $n(\mathbf{r})$ are the hole and electron densities, $C(\mathbf{r}) = N_D^+(\mathbf{r}) - N_A^+(\mathbf{r})$ is the net activated dopant density, and $\mathbf{j}_n(\mathbf{r})$, $\mathbf{j}_p(\mathbf{r})$, $\varphi_n(\mathbf{r})$, and $\varphi_p(\mathbf{r})$ are the electron and hole current densities and the respective quasi-Fermi potentials. The total recombination rate is denoted by R; further details are given below.

The carrier densities are related to the band-edge energies, $E_c^{\mathrm{dd}}(\mathbf{r})$ and $E_v^{\mathrm{dd}}(\mathbf{r})$, and the quasi-Fermi potentials, $\varphi_n(\mathbf{r})$ and $\varphi_p(\mathbf{r})$, via the state equations [33]

$$n(\mathbf{r}) = N_c\mathcal{F}\left(\frac{q(\psi(\mathbf{r}) - \varphi_n(\mathbf{r})) - E_c^{dd}(\mathbf{r})}{k_BT}\right), \tag{4a}$$

$$p(\mathbf{r}) = N_v\mathcal{F}\left(\frac{E_v^{dd}(\mathbf{r}) - q(\psi(\mathbf{r}) - \varphi_p(\mathbf{r}))}{k_BT}\right). \tag{4b}$$

Here, N_c and N_v are the effective density of states for the conduction and the valence band, respectively.

For the function $\mathcal{F}$, we use Fermi-Dirac statistics and k_B is the Boltzmann constant. A temperature of $T = 300$ K has been used in all calculations. It is of note that the valence-band-edge energy, $E_v^{dd}(\mathbf{r})$, and conduction-band-edge energy, $E_c^{dd}(\mathbf{r})$, can be described either by a VCA, a VCA including quantum corrections via LLT, or an atomistic random alloy calculation including LLT-based quantum corrections.

Both the effective landscape extracted from LLT and the effective density of states will depend on the choice of effective mass, $m_{e,h}^*$. This will impact the transport properties calculated in the DD model. As already discussed, previous studies have compared directly the TB electronic structure with a single band model, allowing us to calibrate our model. While studying transport, we assume isotropic effective masses for electrons and holes; the mass in each simulation-cell region is shown in Table I, using masses from Ref. [25]. Future studies can investigate the importance of anisotropic masses; in particular, how this influences the energy landscape derived from LLT.

The recombination rates in Eqs. (3b) and (3c) will depend on the overlap of electron and hole wave functions. This could be calculated, in theory, using the wave functions determined by solving the Schrödinger equation. As we have already stressed, this is basically unfeasible in a 3D system where alloy fluctuations are considered. The solution to LLT could be used to approximate the wave function overlaps, as in Ref. [29,34]. Instead, we make the often-used approximation of using the overlap of the

TABLE I. The material parameters used in the different regions of the simulation supercell. Parameters denoted with a dagger ("†") are taken from Ref. [25].

Parameter			Value in each region		
Name		Units	p-GaN	i-InGaN	n-GaN
Doping		cm^{-3}	5×10^{18}	1×10^{16}	5×10^{18}
μ_h	†	cm^2/V s	5	10	23
μ_e	†	cm^2/V s	32	300	200
m_h^*	†	m_0	1.87	1.84	1.87
m_e^*	†	m_0	0.20	0.18	0.20

densities. The total recombination rate in Eqs. (3b) and (3c), R, is calculated using the ABC model [35,36]. Here, R is the sum of the (defect-related) Shockley-Read-Hall, R^{SRH}, the radiative, R^{RAD}, and the (nonradiative) Auger recombination rate, R^{AUG}. An outline of the formalism and choice of parameters for the ABC model can be found in Appendix B and Table II.

The numerical approximation of the van Roosbroeck system is implemented (in 3D) in DDFERMI [37]. We employ the finite-volume method (FVM) and the current is discretized using the SEDAN (excess-chemical-potential) approach [38–40], which yields a thermodynamically consistent flux approximation in the sense of Ref. [33]. The importance of using a thermodynamically consistent flux approximation has been shown in Ref. [41].

IV. RESULTS

In this section, we present the results of our study on the carrier distribution in the above-described (In,Ga)N/GaN MQW systems. First, we consider a VCA in Sec. IV A, where the impact of alloy fluctuations is neglected. This is studied (i) without and (ii) with the inclusion of quantum corrections. In Sec. IV B, as second step, the impact of alloy fluctuations is investigated, including quantum corrections.

A. Carrier transport in (In,Ga)N-based LEDs assuming homogeneous virtual crystals

To examine the impact of random alloy fluctuations on the carrier distribution in an (In,Ga)N/GaN MQW stack, we start with a "standard" 1D-simulation approach, neglecting random alloy fluctuations as a reference. In a first step, we study the system using the commercial software NEXTNANO [42] and focus on the impact that including an electron blocking layer (EBL) has on the results. This is then compared results from DDFERMI. We utilize the same parameter set in both the NEXTNANO and the DDFERMI simulations, allowing for a direct comparison between the results. In NEXTNANO, a self-consistent Schrödinger-Poisson DD calculation is performed, where a $\mathbf{k}\cdot\mathbf{p}$ Hamiltonian is used to calculate eigenstates across the full simulation domain. When including quantum corrections in DDFERMI, LLT is used, which is based on a one-band effective-mass model. So, following the DDFERMI setup, in NEXTNANO we also employ a one-band model for the calculation of the electron and hole densities in Sec. IV A 1. After making a comparison between NEXTNANO and DDFERMI, we analyze the impact of an EBL in Sec. IV A 2. This also allows us to benchmark our LLT-DD approach against commercially available Schrödinger-Poisson DD calculations.

1. NEXTNANO *simulation without EBL*

The calculated radiative-recombination ratio ϱ [see Eq. (1)] for the systems outlined in Sec. II at 50 A/cm^2 is shown in Fig. 4. Turning first to the data without quantum corrections (purple, solid), we find that in the case of the employed VCA continuum-based description, ϱ is small when the deep QW is at the n side [position 1 (n side) in Fig. 2] and larger when the deep well is at the p side [position 3 (p side) in Fig. 2]. Thus, the 1D model *predicts the opposite trend* when compared to experiment [5].

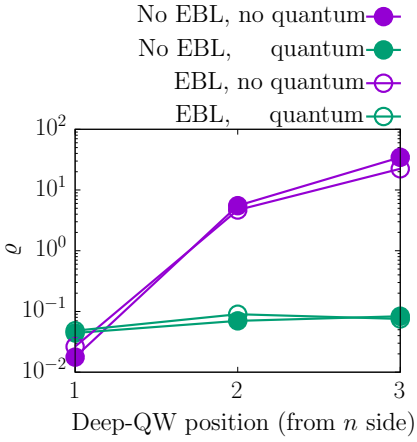

FIG. 4. The ratio of the radiative recombination ϱ [see Eq. (1)] from the shallow wells ($In_{0.1}Ga_{0.9}N$) to recombination from the deep well ($In_{0.125}Ga_{0.875}N$), calculated as a function of the position of the deep well in the MQW stack. Here, ϱ is evaluated using NEXTNANO excluding (purple) and including (green) quantum corrections via a 1-D VCA self-consistent Schrödinger-Poisson drift-diffusion solver; results are shown when excluding (solid, filled circles) and including (dotted, open circles) an $Al_{0.15}Ga_{0.85}N$ blocking layer.

Even when quantum corrections are included via a self-consistent Schrödinger-Poisson DD method, the results for ϱ *excluding alloy fluctuations* do not reflect the results seen in experiment: overall, Fig. 4 (green, solid) reveals that when including quantum corrections in the VCA calculations, the position of the deep QW has little impact on the ratio of the relative radiative recombination, ϱ. These results will be studied in more detail in Sec. IV A 3.

2. Impact of EBL on NEXTNANO *simulations*

To study how the presence of an EBL affects the ratio of radiative recombination ϱ [see Eq. (1)], the systems outlined in Sec. II are simulated with and without a 20-nm $Al_{0.15}Ga_{0.85}N$ EBL using NEXTNANO. The EBL is separated from the p-side QW [position 3 (p side) in Fig. 2] by a 10-nm GaN barrier. Similar settings for an (Al,Ga)N EBL have been used in previous studies [25]. The NEXTNANO calculated ratio of radiative recombination ϱ, when varying the position of the deep QW in the MQW stack, is depicted in Fig. 4 excluding (closed circles) and including (open circles) the EBL.

The inclusion of an EBL does not have a significant impact on the ratio of recombination for both the calculation excluding (purple) and including (green) quantum corrections. As such, this feature of an LED is of secondary importance for the aims of this work.

In general, the EBL needs to be treated as a random alloy. Previous studies of (Al,Ga)N barriers in unipolar device settings have found that the impact of these barriers is lower than what is expected from a 1D simulation for both electrons [43] and holes [44]. Thus, given that our VCA calculations show that the presence of the EBL is of secondary importance for our study, we expect a similar conclusion when treating the EBL with alloy fluctuations. Therefore, it is unlikely that the EBL impacts the result presented here; however, this question may be targeted in future studies.

3. DDFERMI *simulations*

The utilization of commercial software in 1D fails to reproduce the experimentally observed trends. One key element missing from this simulation is the presence of alloy disorder. As such, we next simulate the structures in DDFERMI at a current density of 50 A/cm^2 using (i) a VCA, (ii) a VCA with quantum corrections via LLT, and (iii) a 3D random alloy system including quantum corrections via LLT.

We note that the biases required to simulate a current density of 50 A/cm^2 (approximately 3.1–3.2 V) are slightly higher than observed experimentally [45]. The DD model contains a number of free parameters, such as the electron and hole mobilities. In future, the model could be benchmarked against experimental results in order to get good agreement between the I-V curves, while also including alloy-induced carrier-localization effects.

The calculated radiative-recombination ratio ϱ calculated with DDFERMI is shown in Fig. 5. Again, as in the NEXTNANO studies, the data without quantum corrections and when using a VCA approximation show the *opposite* trend to that observed in experiments. This is illustrated further in Fig. 6(a), which displays the contribution (in percent) to the radiative-recombination rate from each QW (colors) in the MQW stack. The data are shown as a function of position of the deep QW in the MQW system. This confirms that in the VCA case without quantum corrections it is always the QW that is closest to the n-doped side (position 1) that dominates the recombination process; the n-side QW contributes approximately 95% when the deep QW is at position 1 and approximately 70% when the deep QW is at position 2 or 3. Again, we stress that this is the *opposite* trend to the experimental findings in Ref. [5].

To shed more light on this result, the upper row in Fig. 7 depicts the average hole density (black, solid), electron density (black, dashed), and radiative-recombination rate (red) along the c axis when the deep QW ($In_{0.125}Ga_{0.875}N$ well) is (a) closest to the n side (position 1), (b) in the center of the MQW stack (position 2), and (c) closest to the p side (position 3). Focusing on the VCA data, given in Figs. 7(i)(a)–(c), we see the cause of the dominant recombination from the n-side QW: the hole density is always high in this region, independent of which well is closest to the n side. In particular, the p-side QW fails to capture holes effectively and consistently has the lowest hole density. We note that similar behavior is also found in the NEXTNANO calculations discussed in Sec. IV A 1.

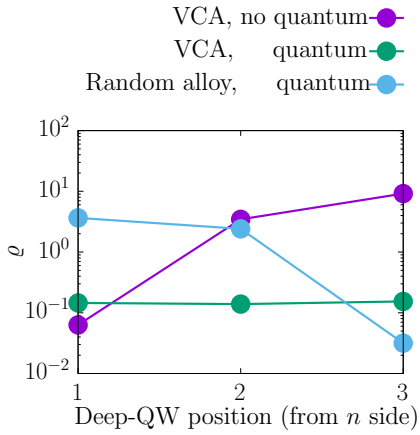

FIG. 5. The ratio of the radiative recombination ϱ [see Eq. (1)] from the shallow wells ($In_{0.1}Ga_{0.9}N$) to recombination from the deep well ($In_{0.125}Ga_{0.875}N$), calculated (using the 3D DDFERMI software) as a function of the position of the deep well in the MQW stack. Here, ϱ is evaluated using DDFERMI excluding (purple) and including (green) quantum corrections via localization-landscape theory (LLT) using a VCA, and a random alloy calculation including LLT-based quantum corrections (blue); these calculations neglect the AlGaN blocking layer.

We saw in Sec. IV A 1 that a VCA including quantum corrections via a self-consistent Schrödinger-Poisson DD calculation does not reflect the result seen in the experiment. Similarly with DDFERMI, including quantum corrections via LLT does not reproduce the observed experimental trends for ϱ. Figure 5 (green) reveals that when including quantum corrections in the VCA calculations, the position of the deep QW has little impact on the ratio of the relative radiative recombination, ϱ. This is similar to findings obtained in Fig. 4 using NEXTNANO. As results between NEXTNANO and DDFERMI without quantum corrections and with corrections from Schrödinger equation (NEXTNANO) or LLT (DDFERMI) agree, this indicates that LLT can provide a good numerically efficient approximation of the Schrödinger equation in DD simulations.

From Fig. 6(b), one can also gain more insight into this behavior and how quantum corrections impact the carrier distribution in the MQW stack. In the *absence* of quantum corrections but utilizing a VCA [Fig. 6(a)], the well closest to the n side dominates the relative radiative-recombination ratio ϱ independent of the position of the

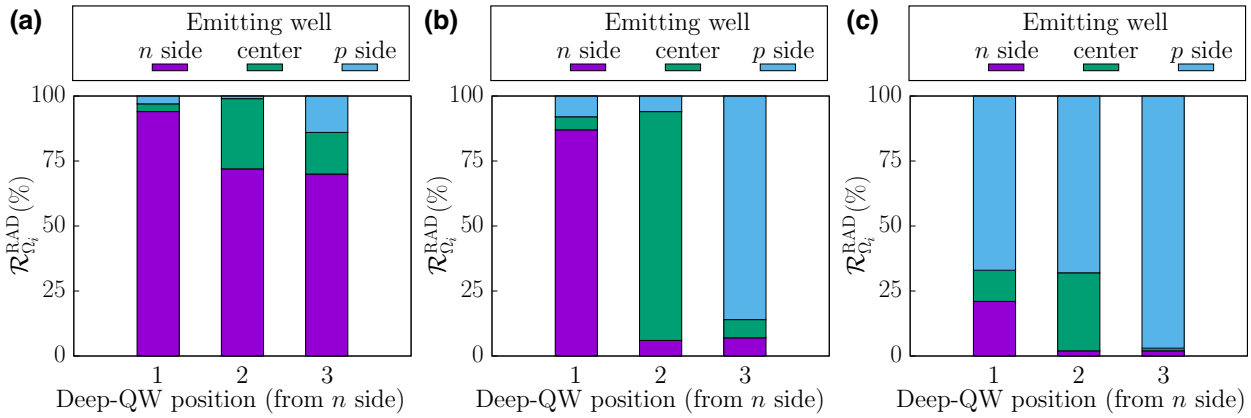

FIG. 6. The contribution of each QW (n side; center; p side) in the (In,Ga)N MQW system to the total radiative recombination $\mathcal{R}^{RAD}_{\Omega_i}$ for $i \in \{n\text{-side}, \text{center}, p\text{-side}\}$ as a percentage of the total radiative recombination from all three QWs for (a) the VCA, (b) the VCA with quantum corrections included via localization-landscape theory (VCA + LLT), and (c) a random alloy calculation including localization-landscape-theory–based quantum corrections (random alloy + LLT). The data are shown as a function of the position of the deep QW (x axis). Each bar contains the percentage recombination from the n-side QW (purple), the center QW (green), and the p-side QW (blue). The labeling is consistent with that introduced in Fig. 2.

deep well in MQW systems. When *including* quantum corrections, this situation is now changed: the deep QW is now the dominant emitter independent of its position in the MQW stack [see Fig. 6(b)].

This behavior becomes clear when analyzing the electron and hole densities as a function of the position of the deep well in the (In,Ga)N/GaN MQWs, as shown in Fig. 7(ii). Looking at the electron densities first, we find that electrons preferentially occupy the well closest to the p side. This effect is enhanced when the deep QW is closest to the p side [cf. Fig. 7(ii)(c)]. In our previous study on unipolar electron transport [21], we have already seen that including quantum corrections leads to a softening of the potential barrier at the QW barrier interfaces. This in turn can lead to an increased electron current at a fixed bias point, when compared to a VCA system without LLT treatment, and thus the electrons can more easily "overshoot" the wells in the MQW system. As a consequence, a lower electron density in the well closest to the n side is observed.

Turning to the hole density, the situation is different. Here, we find that holes preferentially populate the well closest to the n side. Only when the deep QW is closest to the p side is the hole density in this well noticeably increased. However, when comparing the distribution of holes in the MQW as a function of the position of deep well in the absence [Fig. 7(i)] and presence [Fig. 7(ii)] of quantum corrections, the results are not very different. This indicates that quantum corrections, at least when employing a VCA, are of secondary importance for the hole distribution. This finding is consistent with our previous results on unipolar hole transport [22], where we have discussed that due to the high effective hole mass and the small valence-band offset, quantum corrections have a smaller impact on the hole transport when compared to electrons. As a consequence, the distribution of holes follows a similar pattern to that of the VCA where quantum corrections are neglected.

Finally, when looking at the ratio of radiative recombination ϱ, it is important to note that this quantity is not only determined by having both large electron and hole densities in the same well but also by their spatial overlap. As one can infer from Fig. 7(ii)(a)–(c), the largest radiative-recombination rate is always observed in the deepest well. This also indicates that the spatial overlap of electron and hole densities is largest in the deep QW regardless of its position across the MQW system. We again stress that even when including quantum corrections in the VCA calculations, the resulting trend in ϱ does not reflect the trend observed in experimental studies [5].

B. Impact of random alloy fluctuations on the carrier transport in (In,Ga)N/GaN MQWs

In the last step, we move away from the VCA description of the system and also include, in addition to quantum corrections, random alloy fluctuations in the calculations. Figure 5 (blue) shows that—and this time in line with the experimental results by Galler *et. al.* [5]—the deep QW only contributes significantly to the radiative recombination when it is *closest to the p side* (position 3). In fact, when including random alloy fluctuations in the calculations, the well closest to the p side always has the largest contribution to total radiative recombination, as can be seen in Fig. 6(c).

To understand this behavior, Fig. 7(iii) depicts the electron and hole densities in the different wells as a function of the position of the deep well in the MQW systems.

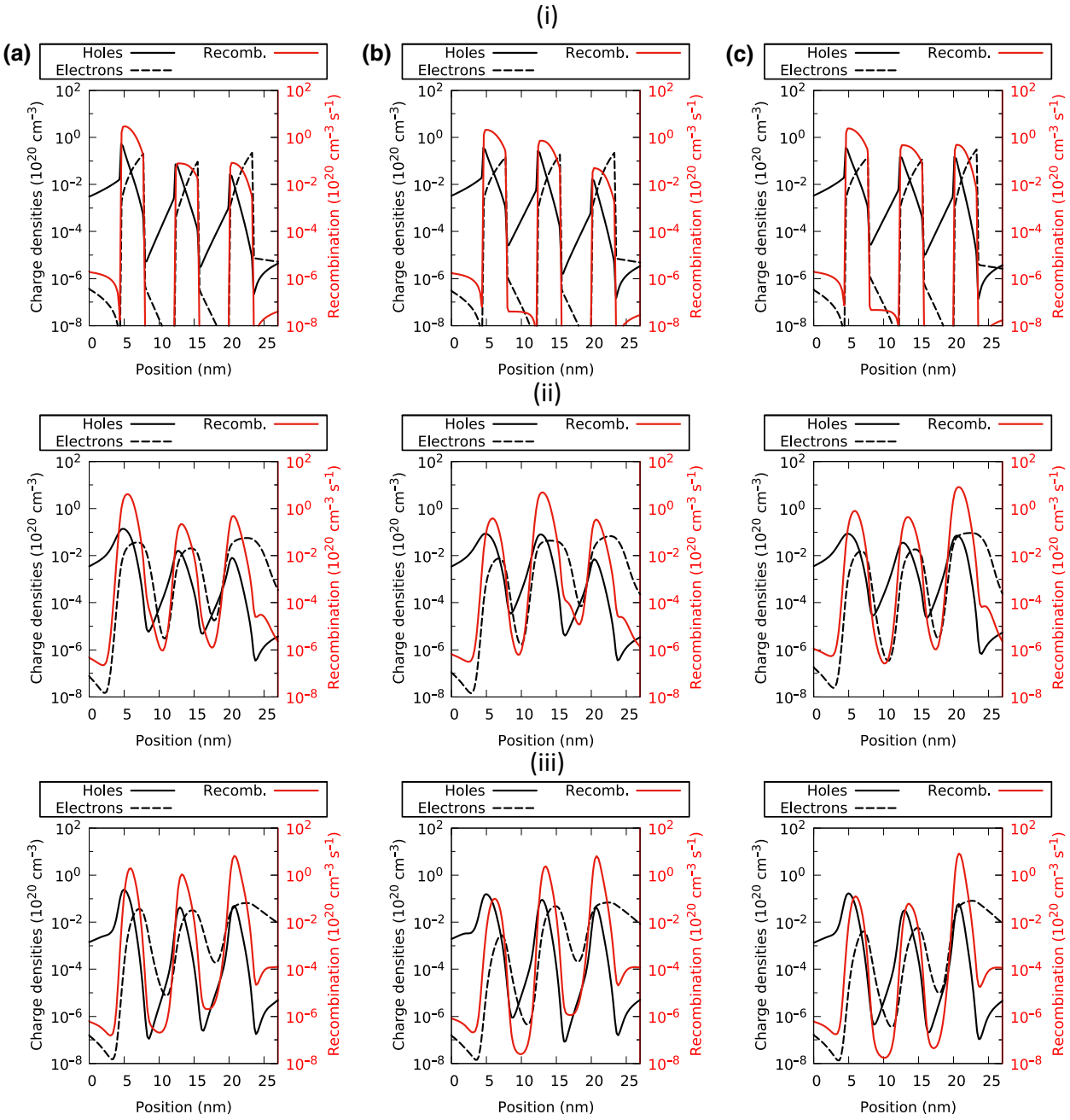

FIG. 7. The hole density (black, solid), electron density (black, dashed), and radiative-recombination rate (red, solid) averaged over each atomic plane along the transport direction. Results are shown from calculations building on (i) a virtual crystal approximation (VCA) (top), (ii) a VCA including quantum corrections via localization-landscape theory (LLT) (center), and a (iii) random alloy description including LLT-based quantum corrections (bottom); the deep well is located (a) at the n side (left), (b) at the center (middle), and (c) at the p side (right). The data are shown on a log scale.

Looking at the electron density first, in comparison to the VCA calculations both including and excluding quantum corrections, random alloy fluctuations lead to a reduction in electron density at the n-side QW. As discussed above and previously, quantum corrections can lead to increased electron transport and including alloy fluctuations adds further to this effect, due to the softening of the barrier at the well interfaces [21]. As a consequence, the electrons can more easily "overshoot" the wells in the MQWs, which can also be seen in the increased electron density beyond the p-side QW when alloy fluctuations and quantum corrections are included. However, in comparison to

the VCA result including quantum corrections, the electron density in the p-side well is only slightly affected by alloy fluctuations.

In contrast, hole densities in the p-side QW are more dramatically changed by alloy fluctuations. As Figs. 7(ii) and 7(iii) show, in comparison to the VCA description, alloy fluctuations lead to an increase in the hole density in the *p-side QW* (position 3) even when the deep QW is closest to the n side (position 1) or in the center (position 2) of the MQW system. While the smoothing of the well barrier interface can increase hole transport, as in the case of electrons, there are now also alloy-disorder-induced localization effects to contend with. As discussed in our previous work, these localization effects are *detrimental* to hole transport [22] and result in an increased hole density in the p-side QW. As a consequence, the well closest to the p side dominates radiative recombination, regardless of the position of the deep well.

We note that there is still a reasonable hole density present in the n-side QW [Fig. 7(iii)(a)–(c)]. In general, the distribution of carriers will also depend on the GaN barrier width and a 5-nm barrier is narrow enough to allow for some hole transport across the MQW [7]; a similar dependence of hole transmission on the barrier width has been seen in previous nonequilibrium Green's function studies [20]. Thus we expect that increasing the barrier width will mainly lead to a reduction of the hole density in the well furthest away from the p side but should affect the hole density in the well closest to the p side to a lesser extent. Therefore, even for a larger barrier width than 5 nm considered here, we expect that the recombination will still be dominated by the p-side QW.

The framework that we have presented is capable of reproducing trends observed in experiments of similar studies. As such, we can now simulate LED structures while targeting the question of higher efficiency. Our results have shown that alloy fluctuations lead to holes getting more easily trapped in the p-side QW. Therefore, increasing the number of QWs in an MQW stack may not lead to increased device performance: even though the active volume is increased, there is a lack of free holes to contribute to recombination. On the other hand, due to the strong polarization field in III-N c-plane QWs decreasing the electron-hole overlap, increasing the well width may not lead to an increase in efficiency either. We have seen above that changing the well composition can impact the carrier distribution across a MQW stack. This may provide an avenue of study aimed at increasing device efficiency. The model employed here can be used to guide such experiments, as well as investigating the impact of various barrier or well widths and compositions.

The framework is also transferable to other material systems in which alloy disorder plays an important role. For example, (Al,Ga)N/(Al,Ga)N QW systems emitting in the UV part of the spectrum can be targeted, where disorder occurs in both the well and the barrier—in such systems, one would expect that carrier transport and recombination will also be impacted by alloy disorder.

V. CONCLUSIONS

In this work, we have applied a 3D quantum corrected multiscale simulation framework to gain insight into the impact of random alloy fluctuations on the electron and hole distribution across the active region of an (In,Ga)N/GaN LED. To investigate the spatial distribution of carriers, we have followed literature experimental studies [5] and analyzed the radiative-recombination ratio in a MQW system, where one of the wells in the system has a higher indium content (deeper well) and its position is varied within the stack. Our benchmarking with commercial software reveals that a "standard" VCA Schrödinger-Poisson drift-diffusion is replicated well with the VCA Schrödinger-LLT drift-diffusion approach, allowing for more efficient calculations.

Equipped with this model our analysis reveals that including (random) alloy fluctuations in the calculations is vital for reproducing trends seen in experiment. More specifically, when using the widely employed VCA, the hole density in the well closest to the p-doped region of the device is reduced compared to our atomistic random alloy calculation—the reduction is strongest (approximately one order of magnitude) when the deep well is not also located at the p side.

As a consequence, and in contrast to the experiment, in the VCA the well closest to the p side contributes very little to the radiative-recombination process, an effect that can be reduced by accounting for quantum corrections. While this leads to enhanced radiative recombination from the well closest to the p side, at least when this well is the deep well, it still does not reflect the trends observed in the experimental studies. However, when including random alloy fluctuations and quantum corrections in our 3D simulation framework, these effects lead to an increase in the hole density in the well closest to the p side. This is due to carrier localization, which traps holes in the p-side QW. Consequently, this well dominates the radiative-recombination process, in line with the experimental data. We note that in addition to quantum corrections and alloy fluctuations, no further ingredients are required (e.g., a multipopulation model) to explain the experimentally observed trends. Therefore, our calculations highlight that alloy fluctuations are a key ingredient in simulations guiding the design of III-N based devices. Thus, the model developed here presents an ideal starting point for future calculations.

ACKNOWLEDGMENTS

This work has received funding from the Sustainable Energy Authority of Ireland and the Science Foundation Ireland (Grants No. 17/CDA/4789, No. 12/RC/2276 P2,

and No. 21/FFP-A/9014) and the Deutsche Forschungsgemeinschaft (DFG) under Germany's Excellence Strategy EXC2046: MATH+, project AA2-15, the Leibniz competition 2020 (NUMSEMIC, J89/2019), as well as the Labex CEMPI (ANR-11-LABX-0007-01) and the Austrian Science Fund (FWF) project 10.55776/F65.

APPENDIX A: MESH GENERATION

The generation of the energy landscape to be used in the active region, e.g., the (In,Ga)N/GaN MQW system, has been outlined in Sec. III A. Now, a full device mesh including the n- and p-doped regions needs to be constructed on which the DD equations are solved. To achieve this, we proceed as follows and divide the device mesh into two regions: an atomistic and a macroscopic one. The atomistic region is used to describe the MQW region and has as many grid points as there are atoms in the system. These points contain information about the conduction- and valence-band-edge energies calculated from TB, as discussed above.

In order to capture the effects of carrier localization in the calculations, the in-plane dimensions of our 3D simulation cell should be larger than the localization length of the holes, given that electrons are less strongly affected by alloy fluctuations [17]. In our atomistic calculations, we use a system with in-plane dimensions of $12.8 \times 11.0\ \mathrm{nm}^2$. This is large enough to see the effects of hole localization, as the in-plane hole localization length for $In_{0.1}Ga_{0.9}N$ QWs is of the order of 1 nm [46]. The in-plane dimensions can be seen in Figs. 3(a) and 3(b), where the in-plane valence- and conduction-band edges of an $In_{0.1}Ga_{0.9}N$ QW are shown. In case of the VCA, given that there are no variations in material properties (band-edge energies) within the growth plane (c plane), a much smaller in-plane area is sufficient ($1.3 \times 1.1\ \mathrm{nm}^2$), which reduces the numerical effort.

LLT is solved on this (finite-element) mesh using a finite-element method (FEM). The DD calculations are carried out employing a Voronoi finite-volume method (FVM) [33]. Therefore, the generated FEM mesh must be transferred to an appropriate FVM mesh. Every point from the FEM mesh is included on the FVM mesh, as well as extra points required to produce a boundary-conforming Delaunay tetrahedral mesh; conduction- and valence-band data are then interpolated onto these additional nodes. This mesh is then embedded within a macroscopic device mesh that contains information about the p- and n-doped regions. In our atomistic transport studies, we focus on systems without an (Al,Ga)N EBL. In principle, an atomistic mesh resolution would be required for the EBL, given the alloy fluctuations in (Al,Ga)N. However, and as we have discussed in Sec. IV A 2 of the main text, an (Al,Ga)N EBL is of secondary importance for the questions targeted in the present study and so we exclude this from our simulation cell. Therefore, outside the active MQW region of the system, pure GaN is assumed. Thus, the conduction- and valence-band-edge values are position independent (except for changes due to an applied bias). The absence of strongly fluctuating band edges in the macroscopic mesh region allows us to use a sparse mesh and scale the simulation to a full device. The mesh is created using TETGEN [47] and the interpolation is handled via the WIAS PDELIB software package [48]. More details on the mesh generation can be found in Ref. [21].

APPENDIX B: RECOMBINATION

As discussed in the main text, recombination is considered using the ABC model. In this case, the SRH rate is obtained from

$$R^{SRH}(\mathbf{r}) = \frac{r(n,p)}{\tau_p\big(n(\mathbf{r}) + n_i(\mathbf{r})\big) + \tau_n\big(p(\mathbf{r}) + n_i(\mathbf{r})\big)}, \tag{B1}$$

the radiative part via

$$R^{RAD}(\mathbf{r}) = B_0 r(n,p), \tag{B2}$$

and the Auger rate is calculated as

$$R^{AUG}(\mathbf{r}) = (C_n n(\mathbf{r}) + C_p p(\mathbf{r}))r(n,p). \tag{B3}$$

In Eqs. (B1)– (B3),

$$r(n,p) = n(\mathbf{r})p(\mathbf{r}) - n_i^2(\mathbf{r})$$

and

$$n_i^2(\mathbf{r}) = n(\mathbf{r})p(\mathbf{r}) \exp\left(\frac{q\varphi_n - q\varphi_p}{k_B T}\right).$$

The above equations require further input, namely, the radiative-recombination coefficient B_0, the Auger recombination coefficients C_p and C_n, as well as the SRH lifetimes τ_p and τ_n. All these parameters will, in principle, carry a composition dependence [49–51]. Furthermore, B_0, C_p, and C_n will also be carrier density dependent [18,52,53]. Here, we follow the widely made assumption that these coefficients are constant across the (In,Ga)N MQW region [23,25]. In the following, we take a weighted average of the parameters calculated in Ref. [49] for an electron and hole density of $3.8 \times 10^{18}\ \mathrm{cm}^{-3}$, which is a good approximation for the average carrier densities in the QWs at a current density of $50\ \mathrm{A/cm}^2$. As our active region consists of two $In_{0.1}Ga_{0.9}N$ QWs and one $In_{0.125}Ga_{0.875}N$ QW, we evaluate the different recombination coefficients as follows:

$$R_i^{\mathrm{eff}} = \frac{2 \times (R_i^{10\%}) + 0.5 \times (R_i^{15\%} + R_i^{10\%})}{3}. \tag{B4}$$

Here, $R_i^x \in \{B_0^x, C_n^x, C_p^x\}$ $(x \in [0.1, 0.15])$ are the radiative recombination, electron-electron-hole, and hole-hole-electron Auger recombination coefficients, respectively.

TABLE II. The material parameters used in the different regions of the simulation supercell. Parameters denoted with a dagger ("†") are taken from Ref. [25]; parameters denoted with a double dagger ("‡") are derived from Ref. [49] as described in the text.

Parameter			Value in each region		
Name		Units	*p*-GaN	*i*-InGaN	*n*-GaN
τ_p	†	s	10	1×10^{-7}	7×10^{-10}
τ_n	†	s	6×10^{-10}	1×10^{-7}	10
B_0	‡	cm^3/s	2.8×10^{-11}	2.8×10^{-11}	2.8×10^{-11}
C_p	‡	cm^6/s	5.7×10^{-30}	5.7×10^{-30}	5.7×10^{-30}
C_n	‡	cm^6/s	1×10^{-31}	1×10^{-31}	1×10^{-31}

As there are no values for an $In_{0.125}Ga_{0.875}N$ QW in Ref. [49], a linear average of the coefficients in $In_{0.1}Ga_{0.9}N$ and $In_{0.15}Ga_{0.85}N$ wells has been used. A summary of the material parameters employed in all simulations is given in Table II.

[1] C. J. Humphreys, Solid-state lighting, MRS Bulletin **33**, 459 (2008).

[2] M. Usman, M. Munsif, U. Mushtaq, A.-R. Anwar, and N. Muhammad, Green gap in GaN-based light-emitting diodes: In perspective, Crit. Rev. Solid State Mater. Sci. **46**, 450 (2021).

[3] H. Amano *et al.*, The 2020 UV emitter roadmap, J. Phys. D: Appl. Phys. **53**, 503001 (2020).

[4] J. H. Zhu, S. M. Zhang, H. Wang, D. G. Zhao, J. J. Zhu, Z. S. Liu, D. S. Jiang, Y. X. Qiu, and H. Yang, The investigation on carrier distribution in InGaN/GaN multiple quantum well layers, J. Appl. Phys. **109**, 093117 (2011).

[5] B. Galler, A. Laubsch, A. Wojcik, H. Lugauer, A. Gomez-Iglesias, M. Sabathil, and B. Hahn, Investigation of the carrier distribution in InGaN-based multi-quantum-well structures, Phys. Status Solidi C **8**, 2372 (2011).

[6] A. David, M. J. Grundmann, J. F. Kaeding, N. F. Gardner, T. G. Mihopoulos, and M. R. Krames, Carrier distribution in (0001)InGaN/GaN multiple quantum well light-emitting diodes, Appl. Phys. Lett. **92**, 053502 (2008).

[7] J. P. Liu, J.-H. Ryou, R. D. Dupuis, J. Han, G. D. Shen, and H. B. Wang, Barrier effect on hole transport and carrier distribution in InGaN/GaN multiple quantum well visible light-emitting diodes, Appl. Phys. Lett. **93**, 021102 (2008).

[8] F. Römer and B. Witzigmann, in *Light-Emitting Diodes: Materials, Devices, and Applications for Solid State Lighting XXI*, Vol. 10124, edited by J. K. Kim, M. R. Krames, L.-W. Tu, and M. Strassburg, International Society for Optics and Photonics (SPIE, San Francisco, United States of America, 2017), p. 101240Y.

[9] E. P. O'Reilly, A. Lindsay, P. J. Klar, A. Polimeni, and M. Capizzi, Trends in the electronic structure of dilute nitride alloys, Semicond. Sci. Technol. **24**, 033001 (2009).

[10] Y. Zhang, A. Mascarenhas, and L.-W. Wang, Statistical aspects of electronic and structural properties in partially ordered semiconductor alloys, Phys. Rev. B **64**, 125207 (2001).

[11] Y. Zhang, A. Mascarenhas, and L.-W. Wang, Non-Bloch nature of alloy states in a conventional semiconductor alloy: $Ga_xIn_{1-x}P$ as an example, Phys. Rev. Lett. **101**, 036403 (2008).

[12] Y. Zhang, A. Mascarenhas, and L.-W. Wang, Interplay of alloying and ordering on the electronic structure of $Ga_xIn_{1-x}P$ alloys, Phys. Rev. B **78**, 235202 (2008).

[13] L.-W. Wang, Calculations of carrier localization in $In_xGa_{1-x}N$, Phys. Rev. B **63**, 245107 (2001).

[14] P. R. C. Kent and A. Zunger, Carrier localization and the origin of luminescence in cubic InGaN alloys, Appl. Phys. Lett. **79**, 1977 (2001).

[15] M. A. Caro, S. Schulz, S. B. Healy, and E. P. O'Reilly, Built-in field control in alloyed *c*-plane III-N quantum dots and wells, J. Appl. Phys. **109**, 084110 (2011).

[16] D. Chaudhuri, M. O'Donovan, T. Streckenbach, O. Marquardt, P. Farrell, S. K. Patra, T. Koprucki, and S. Schulz, Multiscale simulations of the electronic structure of III-nitride quantum wells with varied indium content: Connecting atomistic and continuum-based models, J. Appl. Phys. **129**, 073104 (2021).

[17] D. S. P. Tanner, M. A. Caro, E. P. O'Reilly, and S. Schulz, Random alloy fluctuations and structural inhomogeneities in *c*-plane $In_xGa_{1-x}N$ quantum wells: Theory of ground and excited electron and hole states, RSC Adv. **6**, 64513 (2016).

[18] C. M. Jones, C.-H. Teng, Q. Yan, P.-C. Ku, and E. Kioupakis, Impact of carrier localization on recombination in InGaN quantum wells and the efficiency of nitride light-emitting diodes: Insights from theory and numerical simulations, Appl. Phys. Lett. **111**, 113501 (2017).

[19] P. Dawson, S. Schulz, R. A. Oliver, M. J. Kappers, and C. J. Humphreys, The nature of carrier localisation in polar and nonpolar InGaN/GaN quantum wells, J. Appl. Phys. **119**, 181505 (2016).

[20] M. O'Donovan, M. Luisier, E. P. O'Reilly, and S. Schulz, Impact of random alloy fluctuations on inter-well transport in InGaN/GaN multi-quantum well systems: an atomistic non-equilibrium Green's function study, J. Phys.: Condens. Matter **33**, 045302 (2021).

[21] M. O'Donovan, D. Chaudhuri, T. Streckenbach, P. Farrell, S. Schulz, and T. Koprucki, From atomistic tight-binding theory to macroscale drift-diffusion: Multiscale modeling and numerical simulation of uni-polar charge transport in (In,Ga)N devices with random fluctuations, J. Appl. Phys. **130**, 065702 (2021).

[22] M. O'Donovan, P. Farrell, T. Streckenbach, T. Koprucki, and S. Schulz, Multiscale simulations of uni-polar hole transport in (In,Ga)N quantum well systems, Opt. Quantum Electron. **54**, 405 (2022).

[23] C. Lynsky, G. Lheureux, B. Bonef, K. S. Qwah, R. C. White, S. P. DenBaars, S. Nakamura, Y.-R. Wu, C. Weisbuch, and J. S. Speck, Improved vertical carrier transport for green III-nitride LEDs using (In,Ga)N alloy quantum barriers, Phys. Rev. Appl. **17**, 054048 (2022).

[24] D. Browne, B. Mazumder, Y.-R. Wu, and J. Speck, Electron transport in unipolar InGaN/GaN multiple quantum well structures grown by NH_3 molecular beam epitaxy, J. Appl. Phys. **117**, 185703 (2015).

[25] C.-K. Li, M. Piccardo, L.-S. Lu, S. Mayboroda, L. Martinelli, J. Peretti, J. S. Speck, C. Weisbuch, M. Filoche, and Y.-R. Wu, Localization landscape theory of disorder in semiconductors. III. Application to carrier transport and recombination in light emitting diodes, Phys. Rev. B **95**, 144206 (2017).

[26] S. Schulz, M. A. Caro, C. Coughlan, and E. P. O'Reilly, Atomistic analysis of the impact of alloy and well width fluctuations on the electronic and optical properties of InGaN/GaN quantum wells, Phys. Rev. B **91**, 035439 (2015).

[27] M. A. Caro, S. Schulz, and E. P. O'Reilly, Theory of local electric polarization and its relation to internal strain: impact on the polarization potential and electronic properties of group-III nitrides, Phys. Rev. B **88**, 214103 (2013).

[28] A. Schliwa, M. Winkelnkemper, and D. Bimberg, Impact of size, shape, and composition on piezoelectric effects and electronic properties of In(Ga)As/GaAs quantum dots, Phys. Rev. B **76**, 205324 (2007).

[29] M. Filoche, M. Piccardo, Y.-R. Wu, C.-K. Li, C. Weisbuch, and S. Mayboroda, Localization landscape theory of disorder in semiconductors. I. Theory and modeling, Phys. Rev. B **95**, 144204 (2017).

[30] D. Watson-Parris, M. J. Godfrey, P. Dawson, R. A. Oliver, M. J. Galtrey, M. J. Kappers, and C. J. Humphreys, Carrier localization mechanisms in $In_xGa_{1-x}N$/GaN, Phys. Rev. B **83**, 115321 (2011).

[31] A. Di Vito, A. Pecchia, A. Di Carlo, and M. Auf Der Maur, Characterization of non-uniform InGaN alloys: Spatial localization of carriers and optical properties, Jpn. J. Appl. Phys. **58**, SCCC03 (2019).

[32] W. van Roosbroeck, Theory of the flow of electrons and holes in germanium and other semiconductors, Bell Syst. Tech. J. **29**, 560 (1950).

[33] P. Farrell, N. Rotundo, D. H. Doan, M. Kantner, J. Fuhrmann, and T. Koprucki, in *Handbook of Optoelectronic Device Modeling and Simulation*, Vol. 2, edited by J. Piprek (CRC Press, 2017), Chap. 50, p. 733.

[34] M. Piccardo, C.-K. Li, Y.-R. Wu, J. S. Speck, B. Bonef, R. M. Farrell, M. Filoche, L. Martinelli, J. Peretti, and C. Weisbuch, Localization landscape theory of disorder in semiconductors. II. Urbach tails of disordered quantum well layers, Phys. Rev. B **95**, 144205 (2017).

[35] S. Karpov, ABC-model for interpretation of internal quantum efficiency and its droop in III-nitride LEDs: A review, Opt. Quantum Electron. **47**, 1293 (2015).

[36] J. Piprek, Efficiency droop in nitride-based light-emitting diodes, Phys. Status Solidi (a) **207**, 2217 (2010).

[37] D. H. Doan, P. Farrell, J. Fuhrmann, M. Kantner, T. Koprucki, and N. Rotundo, DDFERMI—a drift-diffusion simulation tool [Weierstrass Institute (WIAS) software], http://doi.org/10.20347/WIAS.SOFTWARE.DDFERMI, 2020.

[38] Z. Yu and R. Dutton, SEDAN III—A one-dimensional device simulator, www-tcad.stanford.edu/tcad/programs/sedan3.html (1988).

[39] C. Cancès, C. Chainais-Hillairet, J. Fuhrmann, and B. Gaudeul, A numerical-analysis-focused comparison of several finite volume schemes for a unipolar degenerate drift-diffusion model, IMA J. Numer. Anal. **41**, 271 (2020).

[40] D. Abdel, P. Farrell, and J. Fuhrmann, Assessing the quality of the excess chemical potential flux scheme for degenerate semiconductor device simulation, Opt. Quantum Electron. **53**, 163 (2021).

[41] P. Farrell, J. Moatti, M. O'Donovan, S. Schulz, and T. Koprucki, Importance of satisfying thermodynamic consistency in optoelectronic device simulations for high carrier densities, Opt. Quantum Electron. **55**, 978 (2023).

[42] S. Birner, T. Zibold, T. Andlauer, T. Kubis, M. Sabathil, A. Trellakis, and P. Vogl, NEXTNANO: General purpose 3-D simulations, IEEE Trans. Electron. Devices **54**, 2137 (2007).

[43] D. A. Browne, M. N. Fireman, B. Mazumder, L. Y. Kuritzky, Y.-R. Wu, and J. S. Speck, Vertical transport through AlGaN barriers in heterostructures grown by ammonia molecular beam epitaxy and metalorganic chemical vapor deposition, Semicond. Sci. Technol. **32**, 025010 (2017).

[44] K. S. Qwah, M. Monavarian, G. Lheureux, J. Wang, Y.-R. Wu, and J. S. Speck, Theoretical and experimental investigations of vertical hole transport through unipolar AlGaN structures: Impacts of random alloy disorder, Appl. Phys. Lett. **117**, 022107 (2020).

[45] Y. Liu, K. Zhang, F. Feng, K.-W. Chan, S.-Y. Yeung, H.-S. Kwok, and Z. Liu, The size and temperature effect of ideality factor in GaN/InGaN multiple quantum wells micro-light-emitting diodes, J. Soc. Inf. Disp. **29**, 948 (2021).

[46] D. S. P. Tanner, P. Dawson, M. J. Kappers, R. A. Oliver, and S. Schulz, Polar InGaN/GaN quantum wells: Revisiting the impact of carrier localization on the "green gap" problem, Phys. Rev. Appl. **13**, 044068 (2020).

[47] H. Si, TetGen, a Delaunay-based quality tetrahedral mesh generator, ACM Trans. Math. Software **41**, 1 (2015).

[48] J. Fuhrmann *et al.*, PDELIB: A finite volume and finite element toolbox for PDEs (Version 2.4.20190405). [Weierstrass Institute (WIAS) Software], http://pdelib.org, 2019.

[49] J. M. McMahon, E. Kioupakis, and S. Schulz, Atomistic analysis of Auger recombination in *c*-plane (In,Ga)N/GaN quantum wells: Temperature-dependent competition between radiative and nonradiative recombination, Phys. Rev. B **105**, 195307 (2022).

[50] J. M. McMahon, D. S. P. Tanner, E. Kioupakis, and S. Schulz, Atomistic analysis of radiative recombination rate, Stokes shift and density of states in *c*-plane InGaN/GaN qunatum wells, Appl. Phys. Lett. **116**, 181104 (2020).

[51] E. Kioupakis, Q. Yan, D. Steiauf, and C. G. Van de Walle, Temperature and carrier-density dependence of Auger and radiative recombination in nitride optoelectronic devices, New J. Phys. **15**, 125006 (2013).

[52] A. David, N. G. Young, C. A. Hurni, and M. D. Craven, Quantum efficiency of III-nitride emitters: Evidence for defect-assisted nonradiative recombination and its effect on the green gap, Phys. Rev. Appl. **11**, 031001 (2019).

[53] A. David, N. G. Young, C. Lund, and M. D. Craven, Review–the physics of recombinations in III-nitride emitters, ECS J. Solid State Sci. Technol. **9**, 016021 (2019).